Delft University of Technology

Effect of porous Cu addition on the microstructure and mechanical properties of SnBi-xAg solder joints

Liu, Yang; Ren, Boqiao; Zhou, Min; Xue, Yuxiong ; Zeng, Xianghua ; Sun, Fenglian; Fan, Xuejun; Zhang, Guoqi

DOI
10.1007/s00339-020-03926-3

Publication date
2020

Document Version
Final published version

Published in
Applied Physics A: Materials Science and Processing

Citation (APA)
Liu, Y., Ren, B., Zhou, M., Xue, Y., Zeng, X., Sun, F., Fan, X., & Zhang, G. (2020). Effect of porous Cu addition on the microstructure and mechanical properties of SnBi-xAg solder joints. *Applied Physics A: Materials Science and Processing*, *126*(9), 1-10. Article 735. https://doi.org/10.1007/s00339-020-03926-3

Important note
To cite this publication, please use the final published version (if applicable).
Please check the document version above.

Copyright
Other than for strictly personal use, it is not permitted to download, forward or distribute the text or part of it, without the consent of the author(s) and/or copyright holder(s), unless the work is under an open content license such as Creative Commons.

Takedown policy
Please contact us and provide details if you believe this document breaches copyrights.
We will remove access to the work immediately and investigate your claim.

This work is downloaded from Delft University of Technology.
For technical reasons the number of authors shown on this cover page is limited to a maximum of 10.

Applied Physics A (2020) 126:735
https://doi.org/10.1007/s00339-020-03926-3

Applied Physics A
Materials Science & Processing

Effect of porous Cu addition on the microstructure and mechanical properties of SnBi-xAg solder joints

Yang Liu[1] · Boqiao Ren[1,2] · Min Zhou[1] · Yuxiong Xue[1] · Xianghua Zeng[1] · Fenglian Sun[2] · Xuejun Fan[3] · Guoqi Zhang[4]

Received: 8 June 2020 / Accepted: 18 August 2020
© Springer-Verlag GmbH Germany, part of Springer Nature 2020

Abstract

The effects of porous copper (P-Cu) on the microstructure, hardness, and shear strength of SnBi, SnBi-0.4Ag, and SnBi-1Ag solder joints were investigated in this paper. The experimental results show that P-Cu frames distribute in the solder bulks and form triangular areas. The addition of P-Cu leads to the microstructural refinement in the enclosed areas by the P-Cu frames in the solder bulks. The average hardness here is increased due to the fine grain strengthening mechanism. The SnBi-1Ag@P-Cu solder bulk shows smaller Bi-rich grains but larger β-Sn dendrites than the other two P-Cu-enhanced solder bulks. Porous Cu exists as a frame structure in the solder joints, which hinders the initiation and propagation of cracks and has a positive effect on the improvement of joint strength. Compared to the SnBi and SnBiAg solder joints, the shear strength of the P-Cu-enhanced solder joints is increased by 15%. The average shear strength of the SnBi-0.4Ag@P-Cu solder joint is 79.34 MPa, which is the highest among all the solder joints investigated in this study.

Keywords Porous Cu · Microstructure · SnBi · Hardness · Shear behavior

1 Introduction

With the development of the electronics industry, the integration and miniaturization of electronic products have become an inevitable trend, which require higher reliability of solder joints [1–5]. This is a huge challenge for the electronic packaging technology [6–9]. At present, Sn58Bi (SnBi) alloy has a low melting point, good wettability, low cost, and high mechanical strength, and is one of the most promising low-temperature solder materials [10–13]. Although Bi-rich grain enhances the mechanical strength, it leads to the poor ductility of the solder joint. These disadvantages limit the application of Sn58Bi solder in the packaging industry [14–16].

Adding a small amount of Ag into SnBi solder can improve the microstructure and mechanical properties of the solder joint. Sun et al. [17] reported that adding 0.4 wt% Ag element or nano-Ag particles in the solder joint can improve the microstructure and performance of the solder joint. Also, the shear strength of the SnBi-nano Ag solder joint is higher than that of the SnBi-0.4Ag and SnBi eutectic solder joints. Liu et al. [18] added 1 wt% Ag into SnBi solder alloy. The experimental results show that the addition of Ag has a positive effect on the grain microstructure refinement. Besides, due to the addition of Ag, the shear strength of the solder joint increases by 13%. Porous metal is widely used in aerospace, new energy, and other industries due to its lightweight, large specific surface area, and other attractive properties [19–24]. It is also used in the research field of bonding and connection. Zaharinie et al. used porous Cu or Ni as the interlayer for the bonding between sapphire and Inconel [25]. The results show that the strength and ductility of the joint between sapphire and Inconel are improved due to the addition of the porous metals. Jamadon et al. [26] studied the effect of porous Cu on the bonding strength of Sn-based

✉ Yang Liu
lyang805@163.com

[1] College of Electrical, Energy and Power Engineering, Yangzhou University, Yangzhou 225127, China

[2] School of Material Science and Engineering, Harbin University of Science and Technology, Harbin 150040, China

[3] Department of Mechanical Engineering, Lamar University, Beaumont, TX 77710, USA

[4] EEMCS Faculty, Delft University of Technology, 2628CD Delft, The Netherlands

Published online: 26 August 2020

solders. It is found that porous Cu addition improves the bonding strength of solder joints.

In this work, porous Cu was added into SnBi, SnBi-0.4Ag, and SnBi-1Ag low-temperature solders, respectively. The influence of porous Cu addition on the microstructure, hardness, and shear behavior of solder joints was investigated.

2 Experimental procedures

Commercial SnBi, SnBi-0.4Ag, and SnBi-1Ag solder pastes were used as the solder materials in this work. The thickness and purity of the porous Cu sheet in this study are 1.0 mm and 99.99%, respectively. The porous Cu is 1.3 mm in length and 1.3 mm in width. The SEM micrograph of the porous Cu is shown in Fig. 1a. The porous Cu has a reticulated structure, and its average porosity is about 91%. The flux-coated porous Cu was immersed in the molten solder for about 5 s, and then was taken out and cooled to ambient temperature. Thereby, the solder@P-Cu composite solder sheet was obtained. The SEM morphology of the solder@P-Cu sheet is shown in Fig. 1b.

The microstructure and constituent of the solder sheets were observed and analyzed by SEM and energy dispersive spectrometer (EDS). The hardness of the solder sheets was evaluated using the SHIMADZU DUH-211S nanoindentation tester. Here, the testing force is 20 mN and the loading speed is 5 mN/s. To study the effect of porous Cu on the shear behaviors of the composite solder joints, the composite sheets were soldered onto the OSP-treated FR-4 printed circuit board (PCB) at 180 °C for 100 s. Here, the size of the Cu pad is 1.3 mm × 1.3 mm, and the height of the solder joint is 1.0 mm. Therefore, the shape of the solder joint is 1.3 mm × 1.3 mm × 1 mm square sheet. The shear test of the solder joint was performed using a RESCH PTR-1000 tester. The shear height was 150 μm and the shear speed was 0.1 mm/s. The shear strength of each sample was an average value of 20 test results.

3 Results and discussion

3.1 Microstructure of the solder joints

Figure 2a shows the microstructure of the SnBi eutectic solder joint. The SnBi solder alloy is a typical eutectic structure, mainly composed of β-Sn (dark area) and Bi-rich (white area) phases. A small amount of tiny Bi-rich grains distributes on the β-Sn grains in the microstructure. As shown in Fig. 2c, the SnBi-0.4Ag solder bulk has a similar eutectic structure to the eutectic SnBi bulk. The enlarged morphology of the structure and the element mapping results in Fig. 3 demonstrate that the Ag element is uniformly dispersed in the β-Sn phase and the Bi-rich phase. According to the research by Sun et al. [17], when the concentration of Ag is low, it mainly exists in solid solution in SnBi matrix. In contrast, the SnBi-1Ag solder bulk in Fig. 2e shows a different microstructure with the other two. The increasing concentration of Ag enlarges the β-Sn grains. Meanwhile, a large amount of Bi-rich dendrites transform into sub-micron Bi particles. According to the element mapping of the SnBi-1Ag solder bulk in Fig. 4, the Ag element was detected. The constituent was confirmed as Ag_3Sn by the EDS results in Fig. 5a. As shown in Fig. 6, Suganuma [27] et al. reported that Ag_3Sn crystallizes as the primary-precipitated phase during the solidification process of SnBi-1Ag solder. With the progress of the cooling process, Bi-rich grains nucleate and grow. Then Sn, Bi, and Ag_3Sn precipitate at the eutectic temperature. As shown in the enlarged morphology of Fig. 2e, another interesting finding is that Ag_3Sn IMC exists at the grain boundaries of the Bi-rich particles. It is deduced that those primary Ag_3Sn grains suppress the growth of the Bi-rich phase and lead to the formation of tiny Bi-rich particles.

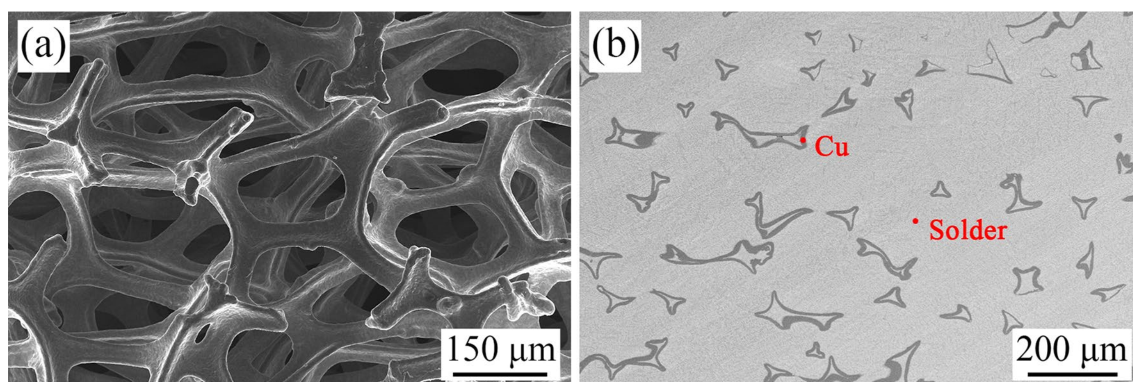

Fig. 1 SEM morphology of the porous Cu and the solder@P-Cu solder sheet. **a** porous Cu and (**b**) solder sheet

Fig. 2 Microstructure of the solder bulks. **a** SnBi, (**b**) SnBi@P-Cu, (**c**) SnBi-0.4Ag, (**d**) SnBi-0.4Ag@P-Cu, (**e**) SnBi-1Ag, and (**f**) SnBi-1Ag@P-Cu

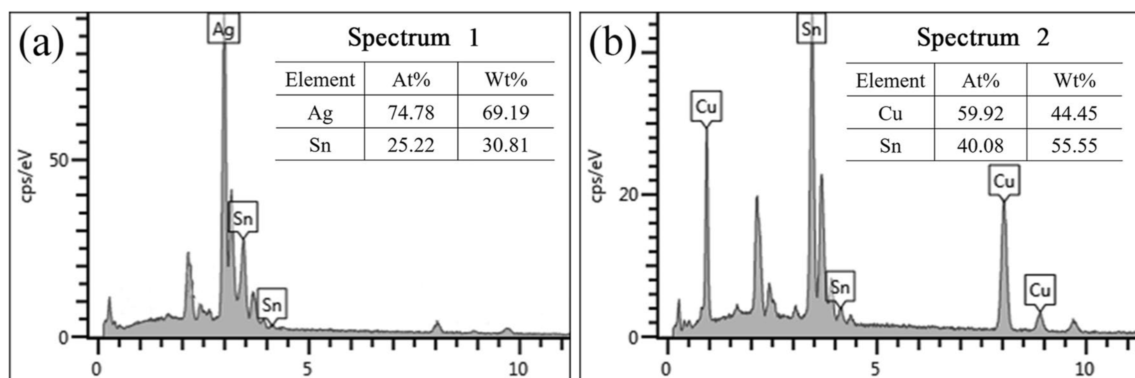

Fig. 3 EDS of the points in Fig. 2. **a** EDS of point 1, (**b**) EDS of point 2

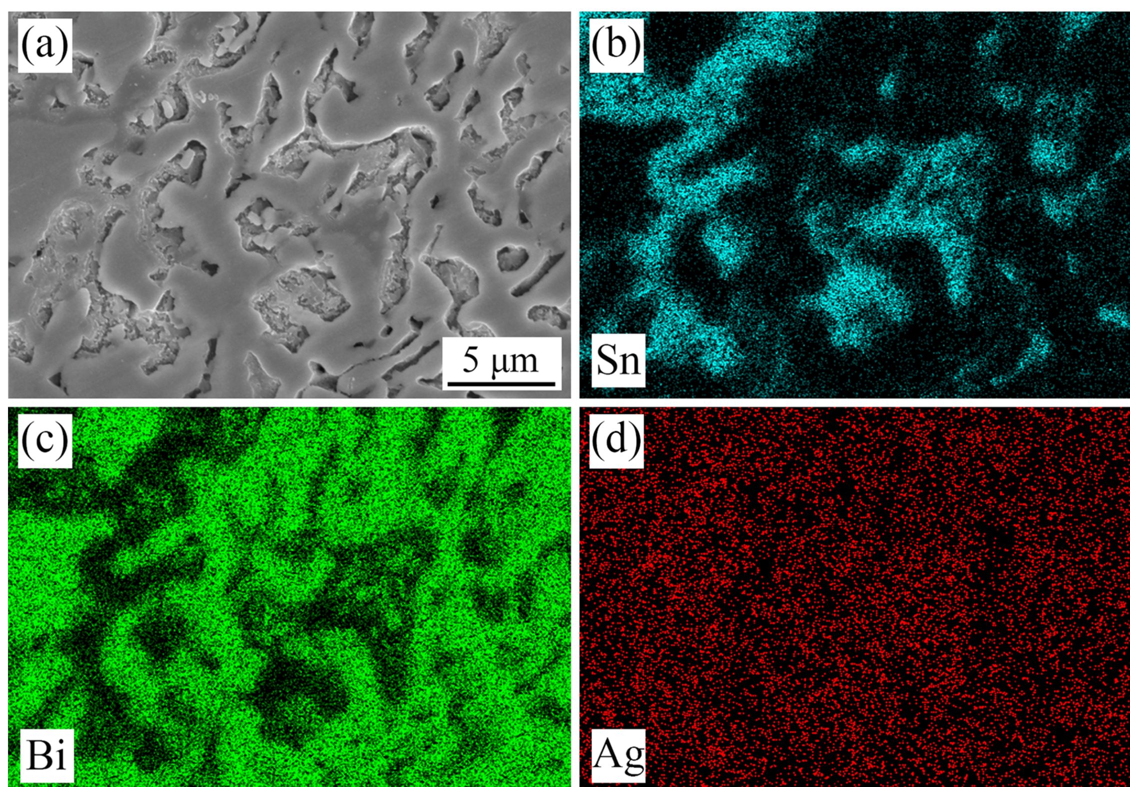

Fig. 4 Microstructure and element mapping of the SnBi-0.4Ag solder bulk. **a** microstructure, (**b**) element mapping of Sn, (**c**) element mapping of Bi, and (**d**) element mapping of Ag

When porous Cu is added into the solder joints, as shown in Fig. 2b, d and f, clear Cu frames can be seen in the microstructures. Cu_6Sn_5 IMC layers are observed between the solder matrix and the Cu frames. The EDS result is shown in Fig. 5b. There are some triangular areas enclosed by those porous Cu frames in the SnBi matrix. It can be seen that the addition of porous Cu has a limited effect on the microstructure outside the enclosed areas. In contrast, the microstructure of SnBi alloy is significantly refined inside those triangular areas. On the one hand, porous Cu frames inhibit the growth of the Bi-rich phase and the β-Sn phase in those areas. On the other hand, due to the dissolution and diffusion of the porous Cu frames, the Cu content in such areas is increased. The dispersed Cu_6Sn_5 IMC grains promote the nucleation of the Bi-rich phase and the β-Sn phase, resulting in the microstructural refinement.

3.2 Interfacial IMC layers of the solder joints

The interfacial morphology of the solder joints is shown in Fig. 7. Thin scallop shape Cu_6Sn_5 IMC layers are observed at the interfaces between the solder bulks and the Cu substrates. The constituent of the IMC is shown in Fig. 7g. As presented in Fig. 7a, c, the IMC layers in SnBi/Cu and SnBi-0.4Ag/Cu solder joints have similar thickness and morphology. In contrast, the SnBi-1Ag/Cu solder joint shows larger Cu_6Sn_5 IMC grains than the other two at the soldering interfaces. The previous discussion indicates the effect of Ag content on the microstructure of SnBi solder bulks. The SnBi-1Ag solder bulk has a different microstructural morphology than the other two. The interfacial morphology of those solder joints is closely related to the microstructure of the solder bulks. For SnBi and SnBi-0.4Ag, the coarsened Bi-rich phase decreases the contact area between the β-Sn phase and the Cu substrate. It hinders the diffusion of Cu and Sn elements at the interfaces and thereby inhibits the growth of the interfacial IMC. In contrast, the SnBi-1Ag solder bulk has small Bi-rich grains but large β-Sn grains. It can be observed from Fig. 7e that some fine Bi-rich particles are embedded in the Cu_6Sn_5 IMC layer at the interface. Although the growth of the IMC at those positions is suppressed, most of the Cu_6Sn_5 grains contact the β-Sn phase and grow into the solder bulk.

As shown in Fig. 7b, d and f, with the addition of porous Cu, the morphology and thickness of the interfacial layer between the solder bulks and the Cu substrates changed. The

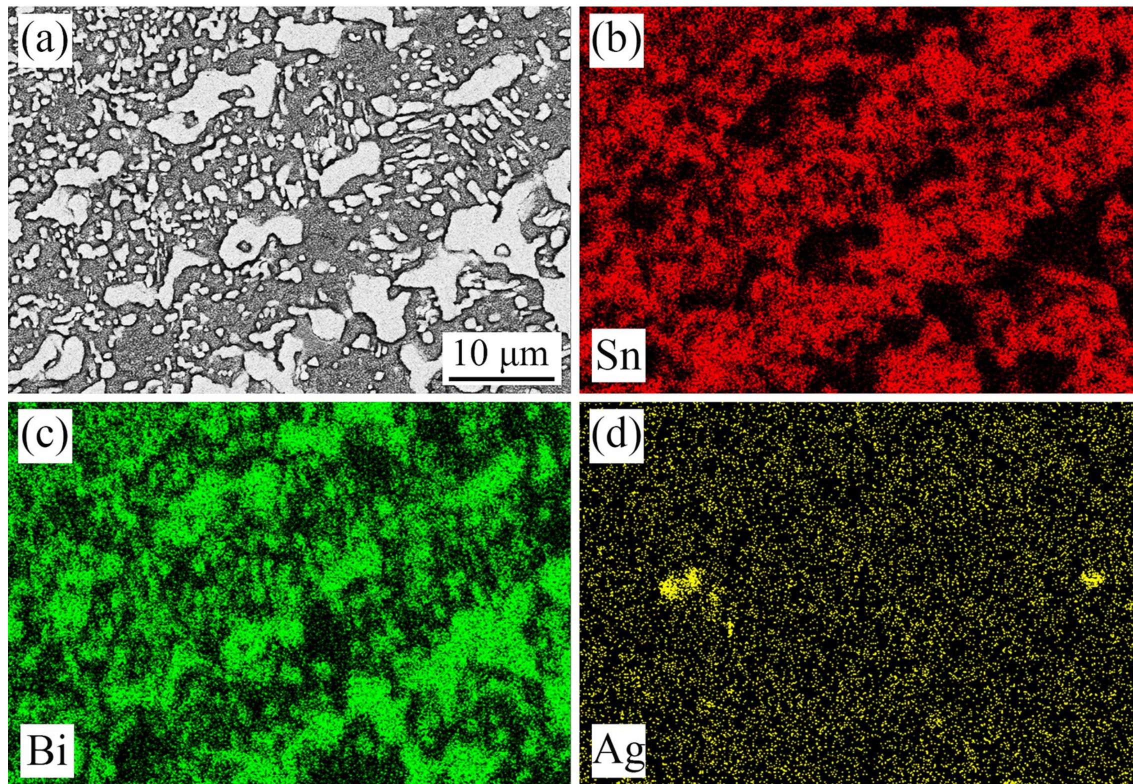

Fig. 5 Microstructure and element mapping of the SnBi-1Ag solder bulk. **a** microstructure, (**b**) element mapping of Sn, (**c**) element mapping of Bi, and (**d**) element mapping of Ag

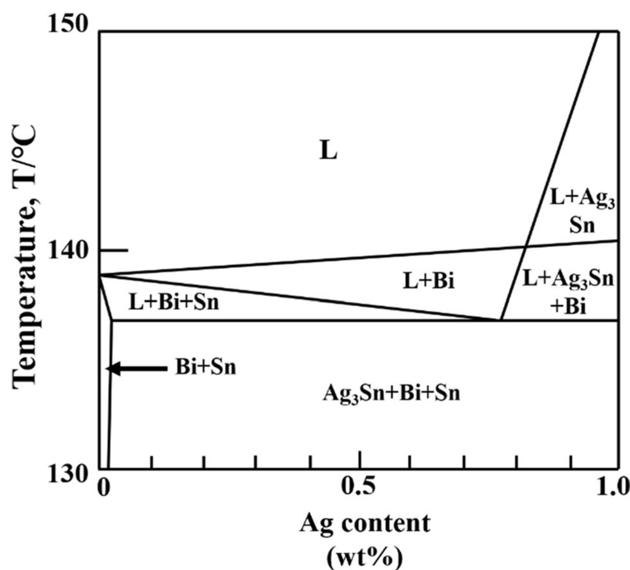

Fig. 6 Phase diagram of Sn-Bi-xAg [27]

IMC thickness in Fig. 8 demonstrates that the effect of the Ag content on the thickness of the IMC is consistent with the solder joint without adding porous Cu. As indicated by the microstructural investigation, the porous Cu addition has a limited effect on the size of Bi-rich and β-Sn grains. The SnBi-1Ag@P-Cu solder joint presents tiny Bi-rich phase and large β-Sn. Consequently, the interfacial IMC shows higher thickness in the SnBi-1Ag@P-Cu/Cu solder joint than that in the others. Also, it can be seen from Fig. 8 that the addition of porous Cu leads to an increase of IMC thickness of the solder joints. As shown by the element mapping of SnBi@P-Cu joint in Fig. 9, the Cu frame here increases the concentration of Cu near the interface of the solder joint. Therefore, the IMC layers in the porous Cu-enhanced solder joints show increased thickness.

3.3 Hardness of the solder bulks

It was found that there are two kinds of areas separated by the porous Cu frame in the solder bulk via microstructural

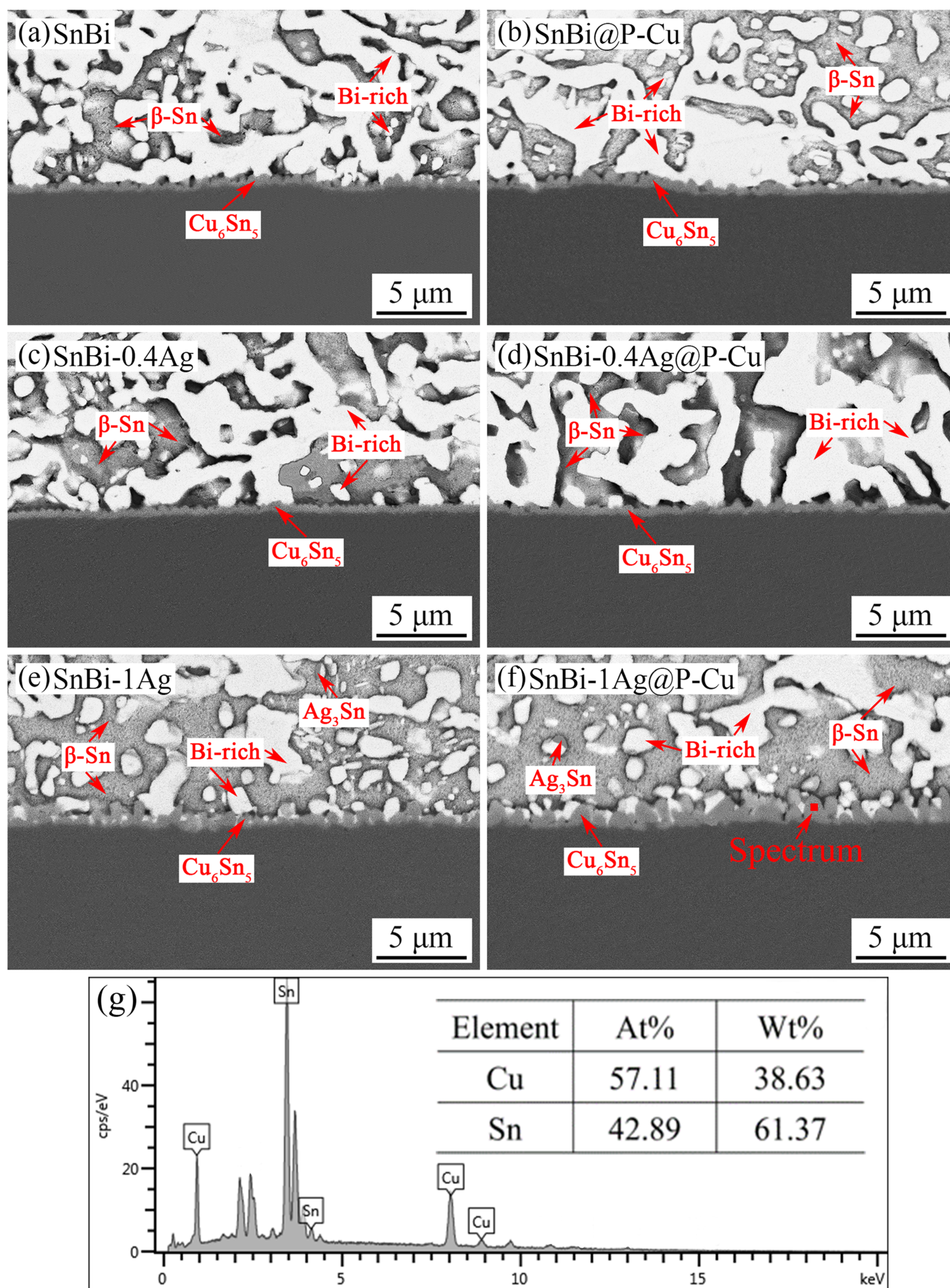

Element	At%	Wt%
Cu	57.11	38.63
Sn	42.89	61.37

Fig. 7 Interfacial microstructure and EDS of the solder joints on Cu subsrtate (**a**) SnBi, (**b**) SnBi@P-Cu, (**c**) SnBi-0.4Ag, (**d**) SnBi-0.4Ag@P-Cu, (**e**) SnBi-1Ag, (**f**) SnBi-1Ag@P-Cu, (**g**) EDS result of the IMC in (**f**)

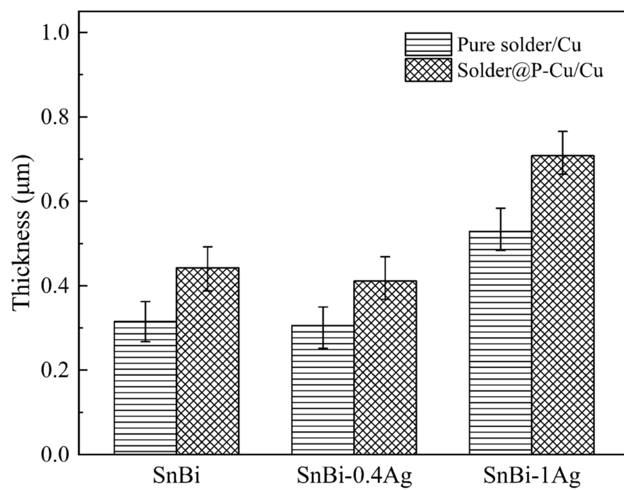

Fig. 8 The thickness of the interfacial IMC layers

observation. Therefore, the indentation test is performed at positions a and b on each solder bulk, as shown in Fig. 10. The hardness of the solder bulks is shown in Fig. 11. As shown in the figure, the SnBi and SnBi-0.4Ag solder bulks show similar hardness with an average of 285.5 MPa. The average hardness of SnBi-1Ag reaches 324.1 MPa, which is higher than that of the other two. According to the microstructure of the solder bulk in Fig. 2e, a large amount of sub-micron Bi-rich particles and Ag_3Sn grains disperse in the SnBi-1Ag solder matrix. The dispersion strengthening of those phases is suggested to be the dominant mechanism for the hardness increase.

As shown in Fig. 11, the addition of porous Cu significantly increases the hardness of position a in the three types of solder joints. Among them, the SnBi-1Ag@P-Cu solder bulk has the highest hardness at position a, with an average of 364.8 MPa. As reported in our previous study [28], this phenomenon is attributed to three factors. First, as shown in Fig. 2b, d and f, it can be found that the position a has finer microstructure than position b as well as the pure solder bulk without porous Cu addition. The microstructural refinement leads to the hardness increase. Second, the diffusion and dissolution of the Cu frames increase the Cu concentration in this area and, thus, affect the hardness. Additionally, the Cu frames have a restraining effect on the enclosed areas and, thus, increase their stress and hardness. As shown in Fig. 10, the addition of porous Cu shows a limited effect on the hardness of position b in the solder bulks. According to the microstructural investigation, the grain size of β-Sn and Bi-rich phases change slightly due to the addition of porous Cu. Therefore, the hardness of position b is similar to that of the pure solder bulks.

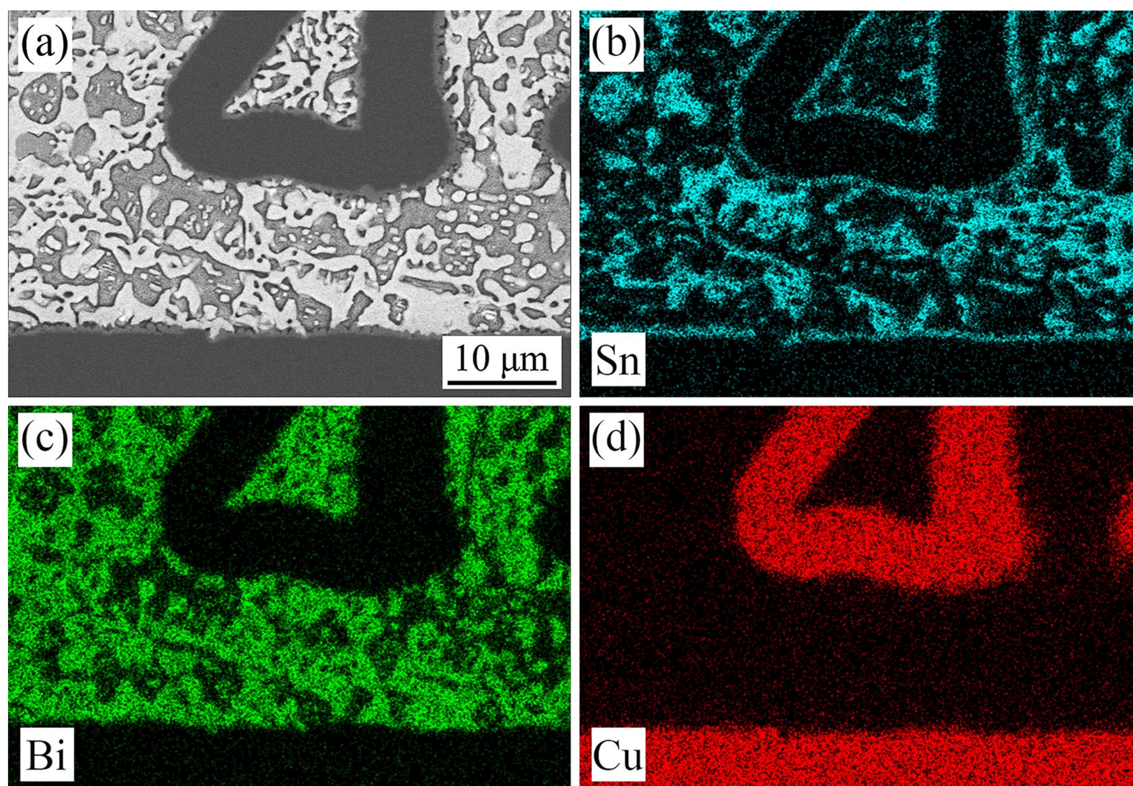

Fig. 9 Microstructure and element mapping of the SnBi@P-Cu solder joint. **a** microstructure, (**b**) element mapping of Sn, (**c**) element mapping of Bi, and (**d**) element mapping of Cu

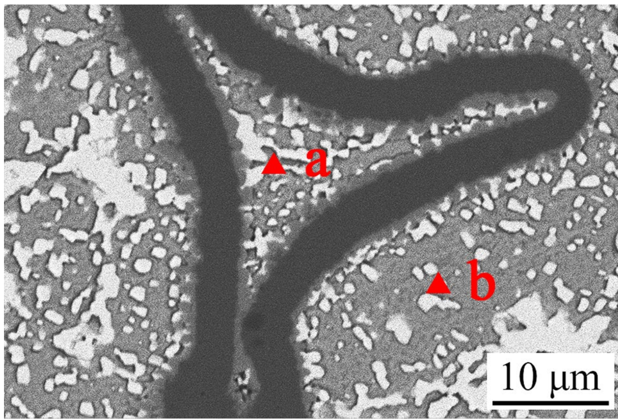

Fig. 10 Microstructure of the SnBi-1Ag@P-Cu solder bulk for nanoindentation test

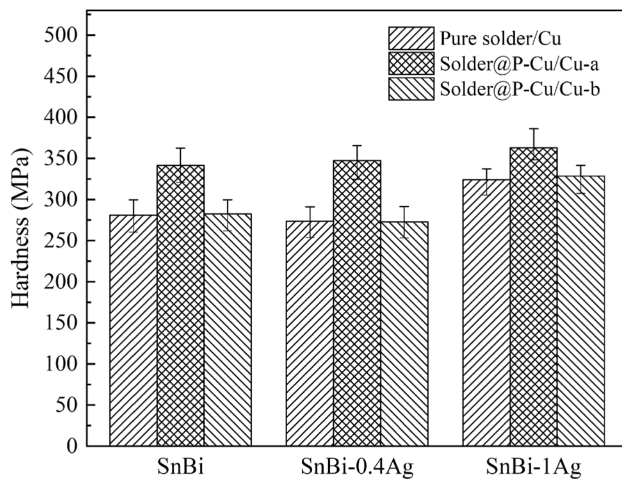

Fig. 11 Hardness of the solder bulks

3.4 Shear behavior of the solder joints

Figure 12 shows the shear strength of the solder joints. Among the three types of solder joints without porous Cu, SnBi-0.4Ag/Cu solder joint showed the highest shear strength, with an average of 68.8 MPa. With the addition of porous Cu, the shear strength of the solder joints increased significantly. Among them, the shear strength of SnBi-0.4Ag@P-Cu solder joint reaches 79.34 MPa, which is increased by 15%.

Figure 13 shows the fracture morphology of SnBi, SnBi-0.4Ag, and SnBi-1Ag solder joints. The enlarged morphology in Fig. 13d, e and f indicates that the three

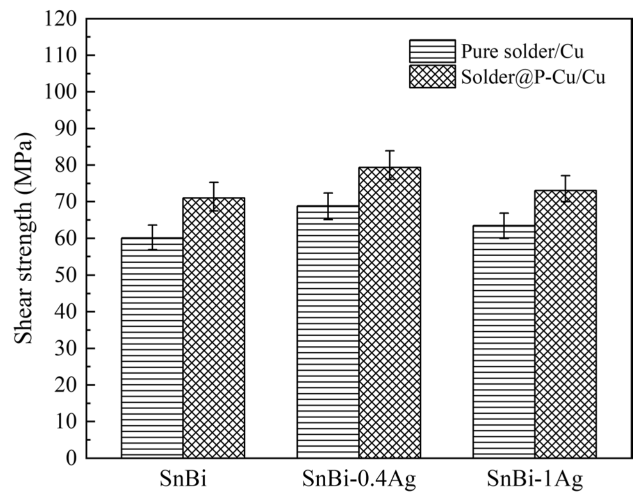

Fig. 12 Shear strength of the solder joints

types of solder joints are mainly brittle fracture. Among them, SnBi and SnBi-0.4Ag solder joints have residue solder bulk on the shear fractures, indicating that their fractures mainly occur in the solder bulk. This shows that the strength difference between the two mainly comes from the strength difference of the solder bulks. Due to the addition of a small amount of Ag, the dispersed Ag_3Sn in the SnBi-0.4Ag solder joints causes the strength increase. According to the element mapping analysis in Fig. 14, Ag_3Sn and Cu_6Sn_5 are found on the shear fracture of SnBi-1Ag solder joint in Fig. 13f. It is clear that when the Ag content in the solder is increased to 1 wt%, the fracture position of the solder joint is changed to the soldering interface. As presented in Fig. 7, SnBi-1Ag solder joint shows coarsened Cu_6Sn_5 IMC layer embedded by Bi-rich particles. Therefore, the main factor for its lower strength than the SnBi-0.4Ag solder joint is the strength decrease at the soldering interface.

Figure 15 shows the shear fractures of the three solder joints enhanced by porous Cu. Compared with the fractures in Fig. 13, the effect of porous Cu on the fracture positions is limited. The solder joints mainly broke due to the brittle failure in the solder bulk or at the interface of the solder joint. As demonstrated by the microstructural observation, the porous Cu frame is continuously and uniformly distributed in the solder bulk. First, porous Cu has the effect of second-phase strengthening in the solder joints. Second, the porous Cu frame is positive on inhibiting the generation and propagation of cracks. Therefore, due to the addition of porous Cu, the shear strength of the three solder joints increases.

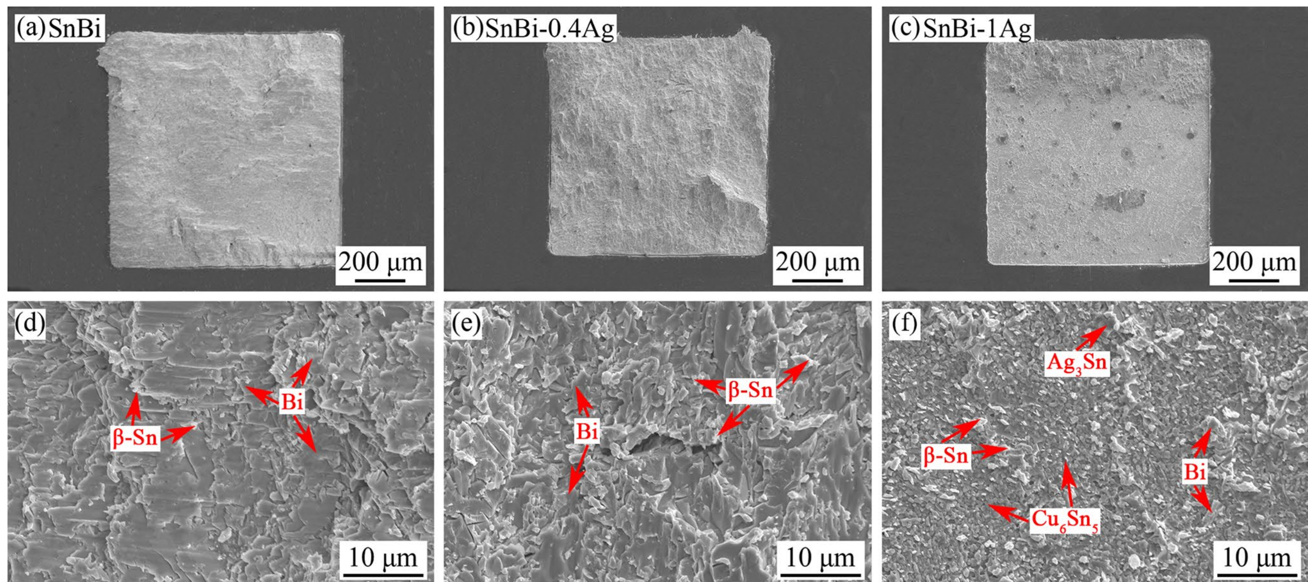

Fig. 13 Shear fractures of the solder joints. **a** SnBi, (**b**) SnBi-0.4Ag, (**c**) SnBi-1Ag, (**d**–**f**) magnified morphology of (**a**–**c**), respectively

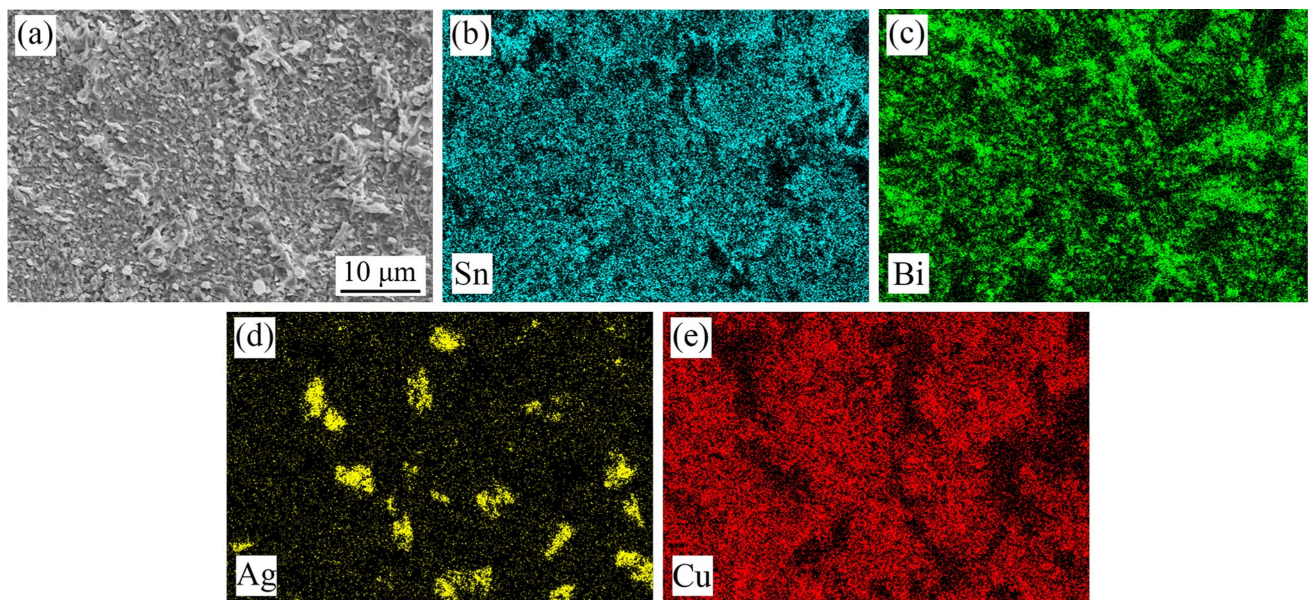

Fig. 14 Elemental mapping of the shear fracture of SnBi-1Ag/Cu. **a** microstructure, (**b**) element mapping of Sn, (**c**) element mapping of Bi, (**d**) element mapping of Ag, and (**e**) element mapping of Cu

4 Conclusion

1. The addition of porous Cu leads to the microstructural refinement in the triangular areas enclosed by the Cu frames, but has limited effect on the microstructure outside of the triangular areas.
2. The addition of porous Cu increases the Cu content in the solder joint as well as the thickness of the interfacial IMC layers.
3. The hardness of the solder bulk in the triangular areas changes slightly due to the addition of porous Cu, while the hardness of the areas inside increases.
4. Porous Cu addition results in increased shear strength of the solder joints. The SnBi-0.4Ag@P-Cu solder joint exhibits the highest shear strength among them.

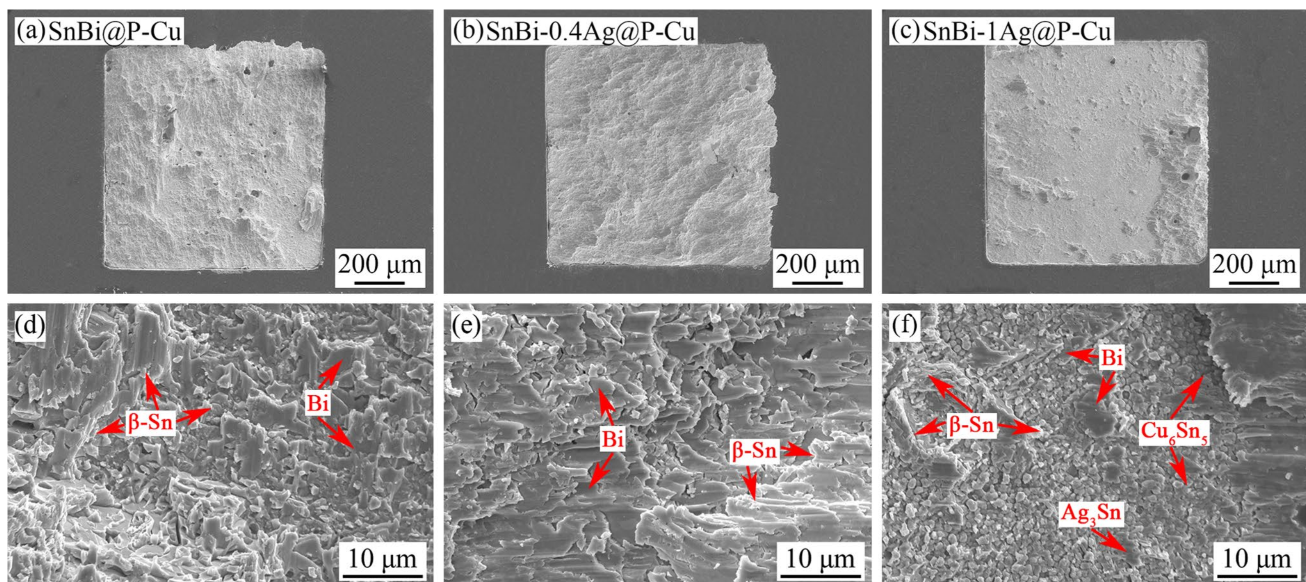

Fig. 15 Shear fractures of solder@P-Cu composite solder joints. **a** SnBi@P-Cu, (**b**) SnBi-0.4Ag@P-Cu, (**c**) SnBi-1Ag@P-Cu. (**d**–**f**) magnified morphology of (**a**–**c**), respectively

Acknowledgements This work is supported by National Natural Science Foundation of China (No. 51604090) and Natural Science Foundation of Heilongjiang Province (No. E2017050).

References

1. L. Yang, W. Zhou, Y. Ma, X. Li, Y. Liang, W. Cui, P. Wu, Mater. Sci. Eng. A. **667**, 368–375 (2016)
2. S. Li, Y. Liu, H. Zhang, H. Cai, F. Sun, G. Zhang, Results. Phys. **11**, 617–622 (2018)
3. J. Cheng, X. Hu, Q. Li, X. Jiang, Appl. Phys. A. **126**, 297 (2020)
4. M. Zhao, L. Zhang, Z. Liu, M. Xiong, L. Sun, N. Jiang, K. Xu, J. Mater. Sci. Mater. Electron. **30**, 15054–15063 (2019)
5. H. Lee, Y. Kim, S. Kim, S. Park, J. Choi, C. Aranas Jr., Small. **14**, 1801349 (2018)
6. X. Zhang, X. Hu, X. Jiang, Y. Li, Appl. Phys. A. **124**, 315 (2018)
7. Y. Xiao, Q. Wang, L. Wang, X. Zeng, M. Li, Z. Wang, X. Zhang, X. Zhu, Ultrason. Sonochem. **45**, 223–230 (2018)
8. J. Lee, D. Kang, S. Kim, M. Son, J. Choi, D. Choi, J. Choi, C. Aranas Jr., J. Materiomics. **4**, 390–401 (2018)
9. Y. Liu, L. Liu, R. Xu, F. Sun, D. Zhu, H. Xu, Mater. Res. Express. **6**, 116328 (2019)
10. O. Mokhtari, H. Nishikawa, Mater. Sci. Eng. A. **651**, 831–839 (2016)
11. L. Yang, G. Wang, Y. Zhang, Y. Xiong, W. Jiang, Appl. Phys. A. **124**, 849 (2018)
12. S. Kim, S. Yeon, J. Kim, S. Park, J. Lee, S. Park, J. Choi, C. Aranas Jr., Y. Son, Acs. Appl. Mater. Interface. **11**, 17090–17099 (2019)
13. X. Hu, H. Qiu, H. Zhang, J. Mater. Sci. Mater. Electron. **30**, 1907–1918 (2019)
14. L. Shen, P. Septiwerdani, Z. Chen, Mater. Sci. Eng. A. **558**, 253–258 (2012)
15. H. Zhang, F. Sun, Y. Liu, J. Mater. Sci. Mater. Electron. **30**, 340–347 (2019)
16. F. Wang, H. Chen, Y. Huang, L. Liu, Z. Zhang, J. Mater. Sci. Mater. Electron. **30**, 3222–3243 (2019)
17. H. Sun, Q. Li, Y. Chan, J. Mater. Sci. Mater. Electron. **25**, 4380–4390 (2014)
18. S. Liu, T. Song, W. Xiong, L. Liu, Z. Liu, S. Huang, J. Mater. Sci. Mater. Electron. **30**, 6701–6707 (2019)
19. S. Choi, S. Kim, J. Yun, Y. Kong, B. Kim, K. Lee, Met. Mater. Int. **17**, 301–307 (2011)
20. Y. Liu, H. Chen, H. Zhang, Y. Li, Int. J. Heat. Mass. Tran. **80**, 605–613 (2015)
21. M. Mirzaee, C. Dehghanian, J. Iran. Chem. Soc. **16**, 283–292 (2019)
22. C. Li, L. Chen, X. Wang, X. Dai, X. Si, J. Qi, Y. Huang, J. Feng, J. Cao, Mater. Lett. **253**, 105–108 (2019)
23. R. Chein, H. Yang, T.H. Tsai, C. Lu, Microsyst. Technol. **16**, 1157–1164 (2010)
24. J. Cheng, H. Song, Y. Pan, Y. Ou, Q. Liu, L. Liu, Ionics **24**, 4093–4099 (2018)
25. T. Zaharinie, R. Moshwan, F. Yusof, M. Hamdi, T. Ariga, Mater. Des. **54**, 375–381 (2014)
26. N. H. Jamadon, F. Yusof, M. H. A. Shukor and T. Ariga, IEEE/CPMT International Electronics Manufacturing Technology Conference, Ipoh, Malaysia, pp. 1–5 (2012). https://doi.org/10.1109/IEMT.2012.6521766
27. K. Suganuma, T. Sakai, K.S. Kim, Y. Takagi, J. Sugimoto, M. Ueshima, IEEE Trans. Electron. Packag. Manuf. **25**, 257–261 (2002)
28. Y. Liu, B. Ren, R. Xu, H. Zhang, F. Sun, Mater. Res. Express. **6**, 116301 (2019)

Publisher's Note Springer Nature remains neutral with regard to jurisdictional claims in published maps and institutional affiliations.